Journal of Biomolecular NMR **27:** 115–132, 2003.

Angular dependence of dipole-dipole-Curie-spin cross-correlation effects in high-spin and low-spin paramagnetic myoglobin**

Guido Pintacuda[a], Karin Hohenthanner[b], Gottfried Otting[a,c] & Norbert Müller[b,*]
[a]*Department of Medical Biochemistry and Biophysics, Karolinska Institute, S-171 77 Stockholm, Sweden*
[b]*Institut für Chemie, Johannes Kepler Universität, Altenbergerstraße 69, A-4040 Linz, Austria*
[c]*Research School of Chemistry, Australian National University, Canberra, ACT 0200, Australia*

Received 8 January 2003; Accepted 16 April 2003

Key words: anisotropy of magnetic susceptibility, dipole-dipole-Curie-spin cross correlation, long-range angle restraints, magnetic susceptibility tensor, paramagnetic relaxation, sperm-whale myoglobin

Abstract

The ^{15}N-HSQC spectra of low-spin cyano-met-myoglobin and high-spin fluoro-met-myoglobin were assigned and dipole-dipole-Curie-spin cross-correlated relaxation rates measured. These cross-correlation rates originating from the dipolar ^{1}H-^{15}N interaction and the dipolar interaction between the ^{1}H and the Curie spin of the paramagnetic center contain long-range angular information about the orientation of the ^{1}H-^{15}N bond with respect to the iron-^{1}H vector, with information measurable up to 11 Å from the metal for the low-spin complex, and between 10 to 25 Å for the high-spin complex. Comparison of the experimental data with predictions from crystal structure data showed that the anisotropy of the magnetic susceptibility tensor in low spin cyano-met-myoglobin significantly influences the cross-correlated dipole-dipole-Curie-spin relaxation rates.

Abbreviations: CN-Mb – cyano-complexed met-myoglobin; CO-Mb – carbonmonoxide-complexed myoglobin; F-Mb – fluoride-complexed met-myoglobin; CSA – chemical shift anisotropy; CSR – Curie spin relaxation; DSA – dipolar shift anisotropy; DD – dipole-dipole; DDxCSA – dipole-dipole-chemical-shift-anisotropy cross correlated relaxation; DDxCSR – dipole-dipole-Curie-spin cross correlated relaxation; PFG – pulsed field gradient.

Introduction

Cross-correlation effects between the dipole-dipole (DD) interaction between ^{1}H and ^{15}N nuclei and the Curie spin of paramagnetic ions contain information about the angle between the H-N bond and the vector connecting the proton with the paramagnetic centre. Due to the long-range effect of paramagnetic relaxation, these angle restraints provide a powerful tool for obtaining long-range structural information (Hus et al., 2000; Bertini et al., 2002a).

Although originating from the dipolar interaction between the nuclear and the thermally averaged electron magnetic moments, Curie-spin relaxation (CSR) acts like a single-spin interaction for the nuclear spins involved (Guéron, 1975; Vega and Fiat, 1976). Consequently, cross-correlation effects between CSR and dipole-dipole relaxation formally behave like cross-correlation effects between chemical shift anisotropy (CSA) and dipole-dipole relaxation (Ghose and Prestegard, 1997).

The first experimental manifestation of dipole-dipole-Curie-spin cross-correlated relaxation (DDx CSR) was by observation of relaxation-allowed coheren- ce-transfer peaks in COSY-type spectra (Bertini et al., 1993; Quin et al., 1993). Subsequently, the mathematical description of DDxCSR was established (Ghose and Prestegard, 1997; Desvaux and Gochin, 1999). In proton NMR spectra this mechanism leads to distinctive multi-exponential relaxation

*To whom correspondence should be addressed. E-mail: norbert.mueller@jk.uni-linz.ac.at
**Dedicated to Professor Richard R. Ernst on the occasion of his 70th birthday.

signatures of methyl singlets (Mandal et al., 2000), which can be quantified to derive angular information (Madhu et al., 2002). DDxCSR effects on the transverse relaxation of $^{1}H^{N}$ single-quantum coherence in ^{15}N-HSQC spectra were reported (Nocek et al., 2000; Madhu et al., 2001) and quantitatively evaluated (Boisbouvier, 1999). Finally, protocols were implemented that allow the use of experimentally derived cross-correlation rates as restraints for protein-structure determinations (Hus et al., 2000; Bertini et al., 2002).

Paramagnetic effects on nuclear relaxation are altered when a metal possesses an anisotropic *g* tensor (Vasavada and Rao, 1989; Bertini et al., 1990) or anisotropic susceptibility (Vega and Fiat, 1976). Recently, a theoretical study suggested that the evaluation of DDxCSR effects could be complicated by the presence of anisotropic susceptibilities (Bertini et al., 2001). In the present study, we used ^{15}N-labelled sperm-whale myoglobin as a model system to evaluate the practical consequences and experimental importance of anisotropic susceptibility and the implications on structure determination.

The spin state of the heme iron in myoglobin is modulated by its axial coordination: In the iron ferric (met) state, high-spin and low-spin components are in thermal equilibrium (Cotton and Wilkinson, 1972). This equilibrium can be shifted along the so-called spectrochemical series by ligand exchange. Thus, strong ligands like CN^{-} stabilize the low-spin ($S = 1/2$) form, while the fluoride complex is found in a nearly pure high-spin ($S = 5/2$) state (Beetlestone and George, 1964). In a similar way, the electronic spin state in the ferrous state is $S = 2$ in its oxy-form, while it can be shifted toward the diamagnetic ($S = 0$) state by complexation with CO.

The different complexes have been the subject of numerous investigations and the polypeptide conformation, metal ion coordination geometry and stability, and its electronic and spectroscopic properties are known with great accuracy (Phillips, 2001; Turano and Lu, 2001).

The most complete solution-NMR data are available for the diamagnetic CO ferrous form (Thériault et al., 1994; Ösapay et al., 1994; Jennings et al., 1995), whereas only partial assignments have been reported for the paramagnetic met-myoglobin derivatives (Emerson and La Mar, 1990; Qui et al., 1993; Kao and Lecomte, 1993; Tolman et al., 1995; Nguyen et al., 1999). In the present study, we established more complete resonance assignments of the ^{15}N-HSQC spectra of CN-met-myoglobin (CN-Mb) and F-met-myoglobin (F-Mb) and used them to refine the previously reported susceptibility tensors. The susceptibility tensors of these two paramagnetic molecules are very different, with a pronounced anisotropy in the case of CN-Mb. Combined with their crystal structures (Kachalova et al., 1999; Bolognesi et al., 1999; Aime et al., 1996), most of which are at high resolution, these complexes provide a useful model system to explore the DDxCSR effects arising from different electronic spin states.

Materials and methods

Preparation of the NMR samples

^{15}N-labelled sperm whale aquo met-myoglobin was prepared as described previously (Jennings et al., 1995). The protocol included reconstitution with unlabelled heme. Since reconstitution initially results in different heme orientations, freshly prepared proteins were kept at 35 °C for 24 h prior to NMR measurements to obtain homogenous samples with a single heme orientation.

A solution of ferric cyano met-myoglobin (CN-Mb) was prepared by addition of a 10-fold excess of KCN to a 2 mM aqueous solution of the aquo complex at pH 8.6 (Emerson and La Mar, 1990). The ferric fluoro met-myoglobin form (F-Mb) was prepared by exchanging a sample of the aquo met-myoglobin solution into a buffer containing 250 mM potassium fluoride (Fluka) and 50 mM potassium phosphate at pH 5.6 (Aime et al., 1996). At lower fluoride concentration (ca. 100 mM), a second set of resonances appeared in the spectrum, which was attributed to the aquo complex, since the same resonances became observable in CO myoglobin samples that had lost some of the CO and had been partially re-oxidized with time. Ferrous CO myoglobin (CO-Mb) was prepared according to Jennings et al. (1995): First, argon gas was bubbled through a solution of aquo met-myoglobin for approximately 30 minutes to remove dissolved oxygen; subsequently, the sample was reduced by the addition of three equivalents of freshly dissolved sodium dithionite (Aldrich) in 0.1 M NaOH, flushed with carbon monoxide (Aldrich), and washed with CO-saturated phosphate buffer in an ultrafiltration device (Millipore). In a last step, all protein solutions were concentrated to approximately 1 mM concentration by ultrafiltration. The final NMR samples contained

50 mM phosphate buffer, pH 5.6, in 90% H_2O/10% D_2O.

NMR spectroscopy

The present results are based on NMR experiments recorded at 30 °C using Bruker DRX-500 and Varian Unity Inova-800 NMR spectrometers, operating at ^1H frequencies of 500 and 800 MHz, respectively. 2D ^{15}N-HSQC experiments were recorded with water-suppression by Watergate (Sklenár et al., 1993), using $t_{1max} = 78.9$ ms and $t_{2max} = 170.6$ ms. 3D NOESY-^{15}N-HSQC (with mixing times of 100, 80 and 40 ms for CO-Mb, CN-Mb and F-Mb, respectively) and 3D TOCSY-^{15}N-HSQC spectra (with mixing times of 60 and 30 ms for CN-Mb and F-Mb, respectively) were recorded using $t_{1max} = 60.0$ ms, $t_{2max} = 45.9$ ms and $t_{3max} = 91.7$ ms and 4 scans per FID. In addition, a 3D TOCSY-^{15}N-HSQC spectrum with 60 ms mixing time was recorded for F-Mb.

T_2 relaxation times of the individual doublet components of the amide H^N resonances were measured by a gradient-selected, generalized ^{15}N-TROSY experiment (Weigelt, 1998), extended by a variable double-spin echo delay T_{relax} before acquisition (Boisbouvier et al., 1999; Figure 1). Two spectra were recorded for each T_{relax} value, selecting either the more shielded or the less shielded components of the H^N doublets by appropriate phase cycling, while always selecting the less-shielded ^{15}N-doublet components. T_{relax} was varied from 6 to 50 ms. No decoupling was applied during data acquisition to avoid any cross-talk from the undesired doublet component.

The cross-correlated relaxation rate η was determined from the difference in relaxation rates of the intensities of the doublet components, $I^{\alpha,\beta}$. Assuming mono-exponential relaxation during the period Δ, $I^{\alpha,\beta}$ evolves with time constant $\lambda \pm \eta$, where λ is the auto-correlated relaxation rate:

$$I^{\alpha,\beta} = I_0^{\alpha,\beta} \exp\{-(\lambda \pm \eta)T_{relax}\}.$$

^{15}N-relaxation times of the CO-Mb sample were measured using the experimental schemes by Farrow et al. (1994).

Data processing, spectra analysis and calculations

Spectra were processed and analyzed with PROSA (Güntert et al., 1992), XEASY (Bartels et al., 1995), nmrPipe/nmrDraw (Delaglio et al., 1995) and nmrView (Johnson and Blevins, 1994).

The ^{15}N-relaxation data were evaluated using Brent's method as implemented in the program Modelfree (Mandel et al., 1995).

All predicted pseudo-contact chemical shifts and cross-correlation rates were calculated using the 1.1 Å crystal structure of sperm-whale Fe^{2+}-myoglobin complexed with CO (Kachalova et al., 1999; PDB code 1BZR). MOLMOL (Koradi et al., 1996) was used to add hydrogens. The reference frame was defined with the origin at the iron, the z-axis perpendicular to the pyrrole nitrogen plane, the x-axis along the N(iii)-N(i) direction and the y-axis along the N(iv)-N(ii) direction (Nguyen et al., 1999). The magnetic susceptibility tensor with the elements χ_{xx}, χ_{yy} and χ_{zz} was oriented by the Euler angles α, β and γ relative to the molecular reference system as shown in Nguyen et al. (1999). As the axes x, y and z can be chosen in an arbitrary manner, up to six pairs of $\Delta\chi_{ax}$ and $\Delta\chi_{rh}$ values can be obtained which are related to one another by circular permutations of the x, y and z axes. The axes were chosen with the largest component along z and the smallest along x (i.e., $|\chi_{zz}| > |\chi_{yy}| > |\chi_{xx}|$).

The axial and rhombic components $\Delta\chi_{ax}$ and $\Delta\chi_{rh}$ (Bertini et al., 2002b) were defined as usual by:

$$\Delta\chi_{ax} = \chi_{zz} - \frac{\chi_{xx} + \chi_{yy}}{2} \quad \Delta\chi_{rh} = \chi_{xx} - \chi_{yy}. \quad (1)$$

Best fits of $\Delta\chi_{ax}$ and $\Delta\chi_{rh}$ and the three Euler angles were obtained by the program PERSEUS (Di Bari et al., 2002) which minimizes the error function

$$t = \sum_i \left[\max\left(|\delta_i^{pcs,calc} - \delta_i^{pcs,obs}| - T_i, 0\right)\right]^2, \quad (2)$$

where $\delta_i^{pcs,obs}$ and $\delta_i^{pcs,calc}$ are the measured and predicted pseudo-contact chemical shifts, respectively, and T_i is a tolerance threshold to allow for experimental uncertainties. The predicted values were obtained from the expression (Bertini and Luchinat, 1996; Bertini et al., 2002b).

$$\delta_i^{pcs-calc} = \frac{1}{12\pi r_{i-Fe}^3}\left[\Delta\chi_{ax}\left(3\cos^2\theta_{i-Fe} - 1\right) + \frac{3}{2}\Delta\chi_{rh}\sin^2\theta_{i-Fe}\cos 2\varphi_{i-Fe}\right], \quad (3)$$

where polar coordinates r_{i-Fe}, θ_{i-Fe}, and φ_{i-Fe} define the position of nucleus i in the metal anisotropy tensor main system. Differences between experimental and calculated shifts were optimized with tolerances T_i of 0.05 and 0.2 ppm for ^1H and ^{15}N chemical shifts,

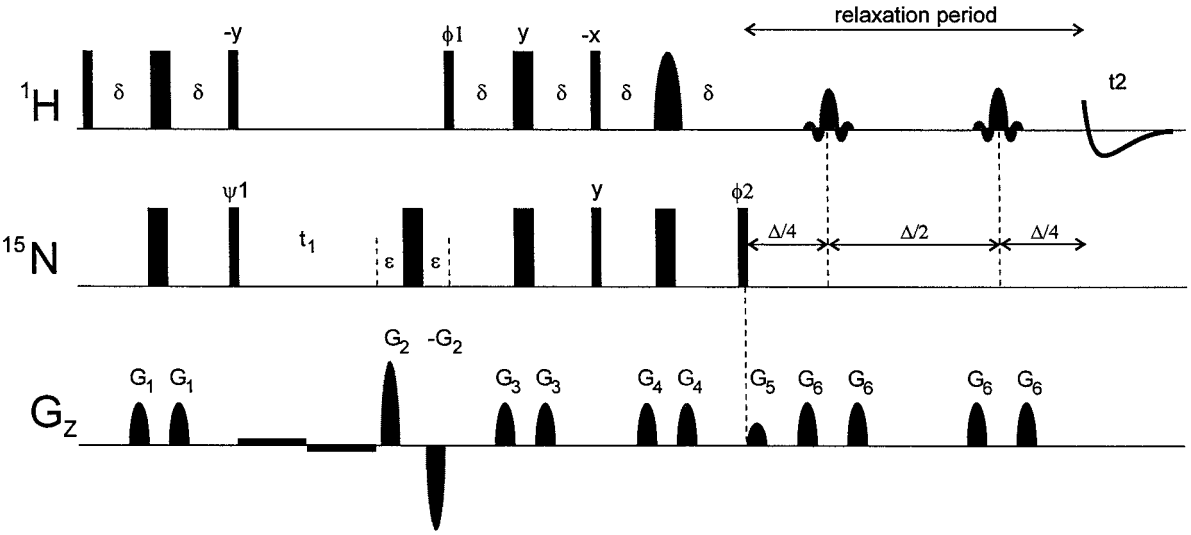

Figure 1. NMR pulse sequence for the measurement of $\eta^{CS,DD}_{HFe,HN}$ relaxation rates. Narrow and large rectangles indicate pulses applied with flip angles of 90° and 180°, respectively. Phases are x unless otherwise indicated. The P-type signal of the lower-right (left) component is selected with ϕ_1/ϕ_2 = y/x (y/−x) and PFG signs as indicated, the N-type signal with ϕ_1/ϕ_2 = −y,−x (−y/x) and inverted sign of the PFGs G_2. The last 180° (^{1}H) pulse before the relaxation period Δ was implemented as a 3-9-19 sequence (Sklenár et al., 1993) for water suppression. In order to refocus chemical shifts and $^3J_{HN,H\alpha}$ coupling evolution during the relaxation period Δ, REBURP-shaped pulses (Geen and Freeman, 1991) were applied centered on the amide protons at 4 ppm offset from the water resonance and calibrated to cover a bandwidth of 6 ppm. Other parameters used were ε = δ = 1.4 ms; τ = 1/(4$^1J_{NH}$) = 2.7 ms. PFGs were applied with a duration of 1 ms and a sine-bell shaped envelope, with the following strengths: $G_{1,2,3,4,5,6}$ = 2, 20, 3, 5, 4.04, 7.3 G/cm, bipolar gradients 0.2 G/cm, all along the z-axis. Phase cycle: ψ_1 = y,−y; receiver = x,−x.

respectively. For axially symmetric tensors, only the three parameters $\Delta\chi_{ax}$, α and β were optimized in the calculation. Calculations of the effects of anisotropic magnetic susceptibility on cross correlation rates were performed with a routine written in Mathematica (Wolfram Research) based on the program Fantacross (Bertini et al., 2001).

Theory

The effect of the dipolar coupling between a paramagnetic center, characterized by a magnetic susceptibility tensor χ, and a nuclear spin located at a position $\boldsymbol{r}$ with respect to the metal center is described by the dipolar shift tensor σ (Bertini et al., 2001, 2002b):

$$\sigma = 3\mathbf{r} \otimes (\mathbf{r} \cdot \chi) - r^2\chi. \tag{4}$$

The isotropic, rank 0 irreducible component of σ represents the spatially averaged nuclear pseudocontact shift (δ^{pcs} in Equation 3), while its rank 2 irreducible component (σ^{DSA}, 'dipolar shift anisotropy') is responsible for the nuclear relaxation (CSR). The symmetry of σ mirrors the shape of the electronic susceptibility tensor χ: when χ is isotropic, σ is traceless and σ^{DSA} axially symmetric, while σ^{DSA} assumes rhombic symmetry when χ becomes anisotropic.

Analogous to the diamagnetic CSA tensor (σ^{CSA}), σ^{DSA} provides non-vanishing cross-correlated spectral density with the DD relaxation mechanism in the ^{1}H-^{15}N system (Ghose and Prestegard, 1997). The cross-correlated relaxation rate due to the interference of the CSR and the DD ^{1}H-^{15}N coupling can be expressed as the product

$$\eta^{DD\times CSR}_{HFe,HN} = \kappa \cdot f(\omega, \tau_c) \cdot \hat{G}, \tag{5}$$

where the constant κ depends on the vacuum permeability μ_0, the magnetic field B_0, Planck's constant $\hbar$, the proton and nitrogen magnetogyric ratios γ_H and γ_N and the H-N distance r_{NH}

$$\kappa = \frac{1}{15}\frac{\mu_0}{4\pi}\frac{B_0\gamma_H^2\gamma_N\hbar}{r_{NH}^3}. \tag{6}$$

The correlation function $f(\omega, \tau_c)$ in the case of isotropic molecular motions is

$$f(\omega, \tau_c) = 4\tau_c + \frac{3\tau_c}{1+\omega_H^2\tau_c^2}. \tag{7}$$

The geometrical factor $\hat{G}$ depends on the relative orientation of the CSR and DD interaction axes; in

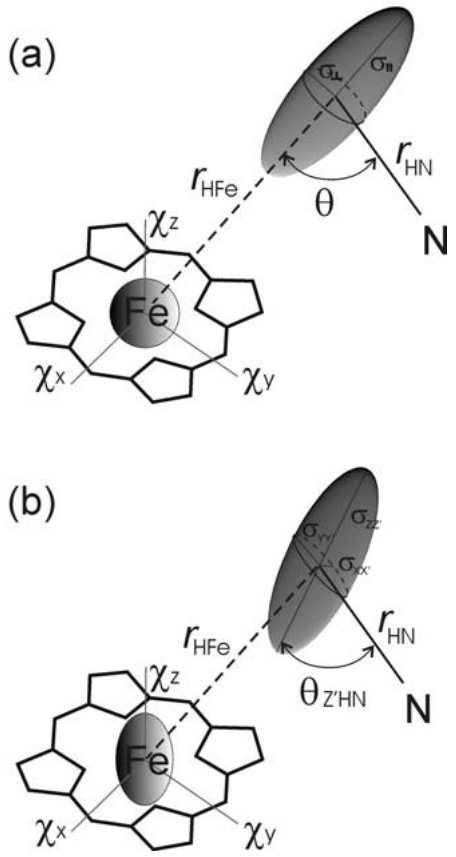

Figure 2. Schematic representation of the $^1H^N$ dipolar shift tensor in the case of isotropic (a) and anisotropic (b) iron magnetic susceptibility. In case (a), the rank 2 irreducible part of the dipolar shift tensor (σ^{DSA}, shaded ellipsoid) is axially symmetric, with the main axis oriented along the H-Fe vector. In case (b), the dipolar shift tensor looses its symmetry and more angles are required to describe its effects on cross-correlated relaxation.

the most general case of rhombically symmetric σ^{DSA} (Goldman, 1984; Bertini et al., 2001), it is expressed as:

$$\begin{aligned}\hat{G}(aniso) &= [\sigma_{xx'} P_2(\cos\theta_{x'HN}) \\ &\quad +\sigma_{YY'} P_2(\cos\theta_{Y'HN}) \\ &\quad +\sigma_{ZZ'} P_2(\cos\theta_{Z'HN})], \end{aligned} \quad (8)$$

where P_2 is the second order Legendre polynomial and the angles $\theta_{X'HN}$, $\theta_{Y'HN}$ and $\theta_{Z'HN}$ specify the directions of the principal axes X', Y' and Z' of the σ^{DSA} tensor (of main values $\sigma_{XX'}$, σ_{YY}, $\sigma_{ZZ'}$) of the ^1H nucleus with respect to the H-N axis (Figure 2b).

In the case of isotropic magnetic susceptibility ($\chi_x = \chi_y = \chi_z = \chi_{iso}$), the dipolar shift tensor σ is axially symmetric ($\Delta\sigma^{DSA} = \sigma_{||} - \sigma_{\perp}$) and the expression for $\hat{G}$ simplifies to

$$\begin{aligned}\hat{G}(\text{iso}) &= \Delta\sigma^{DSA}\ P_2(\cos\theta) \\ &= \frac{3\chi_{iso}}{4\pi\, r_{HFe}^3}\ P_2(\cos\theta), \end{aligned} \quad (9)$$

which contains an easier dependence on the H-N position relative to the metal (r_{HFe} and θ, Figure 2a) (Ghose and Prestegard, 1997).

The principal values of the susceptibility tensor, required for the evaluation of Equations 8 and 9, are not directly measurable by NMR, since the analysis of the pseudocontact shifts only allows determination of the anisotropies ($\Delta\chi_{ax}$ and $\Delta\chi_{rh}$) of the χ tensor. This problem can be circumvented by independently measuring the trace of the tensor (the isotropic susceptibility χ_{iso}), which can be accessed experimentally (e.g., by the Gouy balance method, as in Beetlestone and George, 1964).

The isotropic susceptibility is also related to the effective magnetic moment μ_{eff} (Bertini et al., 2002b) according to

$$\chi_{iso} = \mu_0 \mu_B^2 \mu_{eff}^2 \frac{1}{3kT}, \quad (10)$$

where μ_B is the Bohr magneton, k is the Boltzmann constant and T is the temperature; for species with an orbitally non-degenerate ground state (i.e., a single electron in an orbital which is well separated from any other excited level or multiple unpaired electrons in different molecular orbitals in the absence of strong spin-orbit coupling effects), χ_{iso} can thus be calculated (Bertini et al., 2002b) using

$$\mu_{eff} = g_e \sqrt{S(S+1)}, \quad (11)$$

where $g_e = 2.0023$ and S is the electronic spin quantum number.

Results

Resonance assignment and determination of the magnetic anisotropy

Like in diamagnetic CO-Mb (Thériault et al., 1994), almost all the amide cross-peaks were observable in the ^{15}N-HSQC spectrum of CN-Mb, while the higher electronic spin of F-Mb resulted in broader signals than in CN-Mb and the loss of about 30 resonances (Figure 3).

The strategy for resonance assignments of the paramagnetic myoglobin complexes was based on the

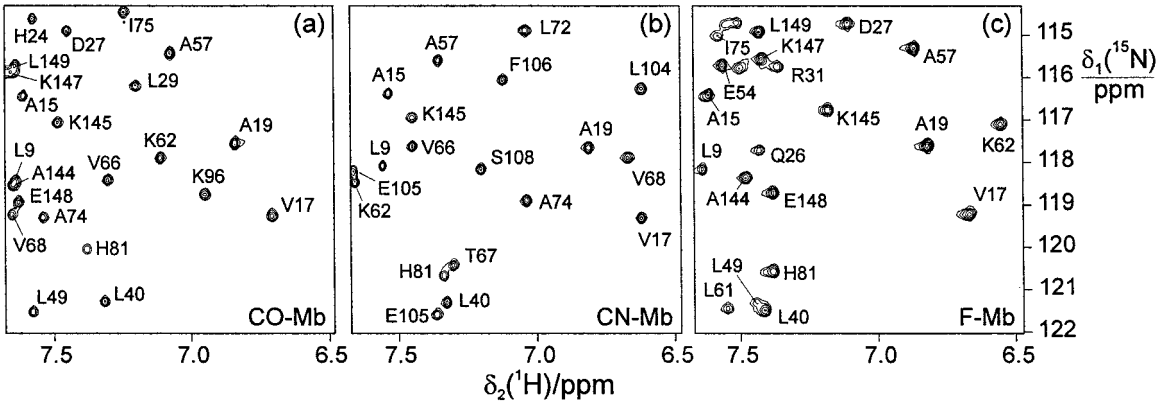

Figure 3. Regions of ^{15}N-HSQC spectra of the three different myoglobin complexes with resonance assignments of backbone amides. The spectra were recorded at 35 °C and pH 5.6 at a ^{1}H NMR frequency of 500 MHz. (a) Diamagnetic CO-Mb; (b) paramagnetic CN-Mb (electron spin 1/2); (c) paramagnetic F-Mb (electron spin 5/2).

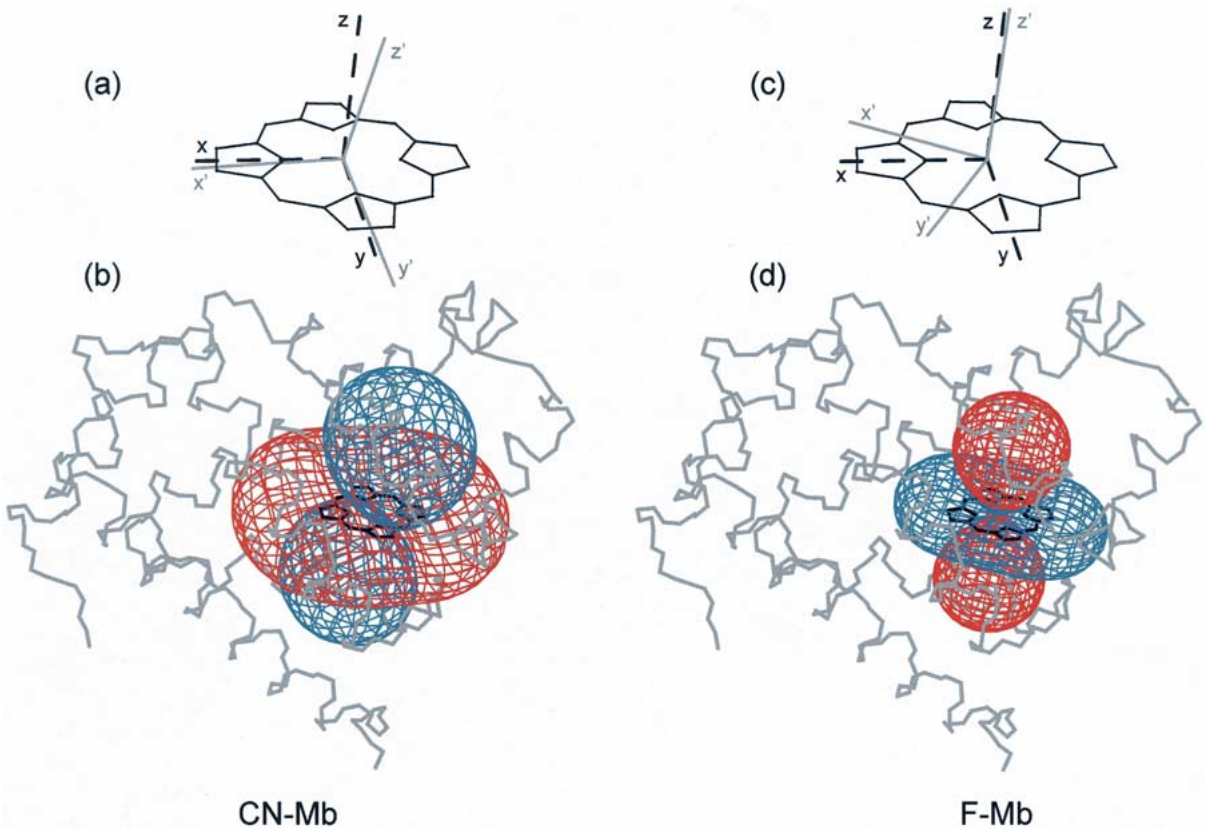

Figure 4. Orientation of the magnetic susceptibility anisotropy tensor in the cyano (left panel) and fluoro (right panel) myoglobins: (a,c) Orientation of the main axes of the tensor (solid lines) relative to the heme reference system (dashed lines); (b,d) iso-surfaces corresponding to a pseudo-contact shift of ±1 ppm superimposed onto a line representation of the protein backbone. Positive and negative shifts are indicated by blue and red wire frames, respectively.

previously determined resonance assignments available for the diamagnetic CO complex at pH 5.6 and 35 °C (Thériault et al., 1994; Jennings et al., 1995). A 3D NOESY-^{15}N-HSQC spectrum resolved ambiguities in crowded spectral regions of CO-Mb. It further allowed the identification of the previously unassigned cross-peaks from Glu52 and confirmed the absence of cross-peaks for Leu86, Lys87 and Glu105.

The ^{15}N-HSQC spectra of the paramagnetic molecules were assigned following the strategy proposed by Tolman et al. (1995). The approach assumes the absence of conformational differences between diamagnetic and paramagnetic myoglobin samples so that any differences in chemical shifts can be attributed to pseudo-contact shifts. In this situation, the magnetic anisotropy susceptibility tensor of the iron can be determined using the protein structure and the chemical shift changes observed for a subset of well-resolved cross-peaks which can be assigned with confidence by comparison with the spectrum of CO-Mb. The susceptibility tensor is used in turn to predict pseudo-contact shifts for all other amides, enabling further resonance assignments and a subsequent refinement of the magnetic anisotropy susceptibility tensor. Both for CN-Mb and F-Mb, availability of the susceptibility tensor reduced the number of assignment possibilities sufficiently that remaining assignment ambiguities could be resolved by inspection of the 3D NOESY-^{15}N-HSQC and TOCSY-^{15}N-HSQC spectra.

In the case of CN-Mb, literature values of the anisotropy and orientation of the susceptibility tensor at pH 8.6 and different temperatures in the range of 5 to 45 °C were available (Emerson and La Mar, 1990; Qui et al., 1993; Nguyen et al., 1999). Similarly, literature values available for aquo (Fe^{3+}) myoglobin (Kao and Lecomte, 1995) were used as starting parameters for the assignment of F-Mb. The approach worked exceedingly well for the assignment of CN-Mb, where the published tensor led to excellent agreement between predicted and observed shifts for amide protons and to good predictions also for ^{15}N chemical shifts, so that the 3D NOESY-^{15}N-HSQC spectrum was sufficient to resolve the assignment of all backbone-amide cross-peaks in the ^{15}N-HSQC spectrum. Remarkably, all cross peaks present in the spectrum of diamagnetic CO-Mb could also be identified for CN-Mb. Large deviations between calculated and observed pseudo-contact shifts were observed in CN-Mb for residue 93 and for residues 48 and 64; His 93 axially coordinates the heme iron and was subsequently excluded due to possible contact-shift contributions, while examination of the 3D NOESY-^{15}N-HSQC spectrum led us to reassign the amides of the other two residues. Our final fit of the susceptibility tensor and the orientation of its main axes is very close to the literature values (Table 1). The tensor is highly anisotropic with the principal axis deviating by about 15° from the heme normal (Figure 4a).

The assignment procedure was more difficult in the case of F-Mb, as the high-spin iron resulted in more substantial line broadening. Cross peaks in the 3D NOESY-^{15}N-HSQC and 3D TOCSY-^{15}N-HSQC spectra were weak and signals from about 30 residues close to the iron were broadened beyond detection. Straightforward comparison of the ^{15}N-HSQC spectra of F-Mb and CO-Mb allowed the assignment of about 50 cross peaks. Initially, the observed pseudo-contact shifts were fitted by an axially symmetric χ tensor with $\Delta\chi_{ax}$, α and β as the only fitted parameters. Combined with the data from the 3D NOESY-^{15}N-HSQC spectrum, the pseudo-contact shifts predicted by this tensor were sufficiently accurate to allow the assignment of more than 80% of the observable ^{15}N-HSQC cross peaks. In the end, only three spectral regions with severe cross-peak overlap could not be assigned. A 3D HNCA spectrum recorded later with a uniformly ^{15}N,^{13}C-labelled sample confirmed the assignments obtained in this way and allowed the assignment of only 10 additional cross-peaks (K. Hohenthanner, G. Pintacuda and N. Müller, unpublished results).

The susceptibility tensor in F-Mb is axially symmetric to good approximation (Table 1). A fit of the pseudo-contact shifts with an anisotropic tensor yielded only a small rhombic component and no significant improvement in the residuals of the fit. In either case, only few nuclei displayed differences between predicted and observed chemical shifts as large as 0.1 ppm and none above 0.3 ppm. Their exclusion from the fit improved the value of the error function but did not alter the determined parameters.

The z-axis of the susceptibility tensor in F-Mb is almost perfectly perpendicular to the heme plane ($\beta \approx 0$, Figure 4c). The isotropic magnetic susceptibility, which is a function of the metal spin S, is approximately 10 times larger than in CN-Mb (Beetlestone and George, 1964), but the magnitude of the anisotropy is much reduced (Figures 3b and d). Interestingly, the signs of the main anisotropy components are opposite for the two different ferric iron spin states, with positive pseudo-contact shifts within the heme plane for the spin 5/2 case and axially above and below this plane for the spin 1/2 case.

Table 1. Principal values $\Delta\chi_{ax}$ and and orientation of the main axes of the magnetic susceptibility anisotropy tensor χ determined in the two paramagnetic samples (columns labeled CN-Mb and F-Mb). The values are compared to reference data available from the literature. For F-Mb, the results obtained assuming axial ($\Delta\chi_{rh} = 0$) and rhombic ($\Delta\chi_{rh} \neq 0$) anisotropy are reported. The Euler angles are referenced according to the convention described in the materials and methods section. In the last row, the value of the isotropic magnetic susceptibility χ_{iso} is indicated for the two samples of low- and high-spin iron; the corresponding values calculated using Equations 10 and 11, i.e. accounting for the electronic spin only, are reported in square brackets

	Low-spin		High-spin		
	CN-Mb	*CN*-Mb[a]	*F*-Mb		*aquo*-Mb[b]
			$\Delta\chi_{rh} = 0$	$\Delta\chi_{rh} \neq 0$	
$\Delta\chi_{ax}$ (10^{-32} m^3)	4.24 ± 0.06	4.25 ± 0.13	-2.49 ± 0.09	-2.58 ± 0.09	-2.31 ± 0.02
$\Delta\chi_{rh}$ (10^{-32} m^3)	-1.02 ± 0.10	-0.98 ± 0.17	–	0.26 ± 0.10	–
α (°)	162 ± 2	150 ± 10	6 ± 5	–	–
β (°)	15.5 ± 0.3	15.8 ± 0.6	-0.7 ± 1.1	-0.7 ± 1.1	0
$\kappa \sim \alpha + \gamma$ (°)	-9 ± 3	-10 ± 5	–	-16 ± 5	–
χ_{iso} (10^{-32} m^3)[c]	4.4 ± 0.5 [2.8]			30.1 ± 0.5 [32.6]	

[a]pH 8.6; Nguyen et al. (1999).
[b]Calculated from the axial zero-field splitting parameter at pH 8.6 and 25 °C reported by Kao et Lecomte (1995).
[c]Extrapolated from variable temperature measurements of Beetlestone and George (1964).

Dipole-dipole-Curie-spin cross-correlation rates

The formalism of Bertini et al. (2001) was used to predict the differential line broadenings in the H^N doublets due to DDxCSR for anisotropic and isotropic susceptibility tensors.

Values of χ_{iso} of the myoglobin complexes are available in the literature (Beetlestone and George, 1964; Cerdonio et al., 1981) and shown in Table 1. While the experimental value of μ_{eff} for F-Mb closely coincides with the value predicted from equation 11 for a pure S = 5/2 state, CN-Mb exhibits an effective magnetic moment μ_{eff} that is 1.3 times larger than expected. This could be explained by non-negligible spin-orbit coupling.

For every amide proton, the proton coordinates and the dipolar shift-tensor components were determined in the metal-anchored susceptibility frame, the tensor was symmetrized (Equation 4 in Bertini et al., 2001) and diagonalized, and the geometrical factor $\hat{G}$ evaluated for each proton using Equation 8 or 9 for the anisotropic and isotropic case, respectively.

In the case of F-Mb, the geometric factors calculated for the anisotropic case, using the fitted values and orientations of the anisotropic χ tensor components (Table 1), were very similar to those calculated for isotropic susceptibility (Figure 5b).

In the case of CN-Mb, however, the geometric factors predicted for the anisotropic and isotropic χ tensors are significantly different. As expected from the general shape of the anisotropic χ tensor (Figure 4), the isotropic approximation is particularly poor for protons in the vicinity of the metal centre, while the effects from anisotropy are less pronounced further away (Figure 5a).

All experimentally determined cross-correlation rates are summarized in Table 2. The measured cross-correlation rates in the two paramagnetic samples (η^F and η^{CN}) are a superposition of DDxCSR and DDxCSA cross-correlation rates. These two cross-correlation effects cannot be separated experimentally. However, availability of the diamagnetic CO-Mb sample allowed the measurement of the dipole-dipole-CSA cross-correlation rates (η^{CO}) and their subtraction from the cross-correlation rates observed in the paramagnetic samples, assuming that differences in DDxCSA cross-correlation rates between the myoglobin complexes are negligible (Figure 6). The DDxCSR rates were thus obtained by subtraction as η^F-η^{CO} and η^{CN}-η^{CO}. This approach is evidently limited by the requirement of availability of a diamagnetic complex. In cases where this is not possible, density functional theory can be used for estimation of chemical shift anisotropy tensors (Sharma et al., 2002; V. Smrecki and N. Müller, unpublished results).

In CN-Mb, the DDxCSR rates ranged from -4 to $+8$ s^{-1}, with measurable effects only up to about 11 Å from the metal (Figure 7a).

The DDxCSR rates obtained for F-Mb were not much larger in magnitude (ranging from -13 to $+10$ s^{-1}), but were observed for amide groups much further away from the metal (Figure 7b). While the

Table 2. Experimental DDxCSR H^N cross correlation rates (s^{-1}) for the three myoglobin samples

		η^{CO} (s^{-1})			η^{CN} (s^{-1})			η^{F} (s^{-1})		
Leu	2	3.5	±	0.5	3.5	±	0.3	4.0	±	0.6
Ser	3	4.8	±	0.4	5.3	±	0.4	6.5	±	0.5
Glu	4	5.5	±	0.4	6.3	±	0.4	5.9	±	0.6
Gly	5	4.5	±	0.7	4.4	±	0.3	4.1	±	0.7
Glu	6	4.1	±	0.5	3.9	±	0.3	4.6	±	0.5
Trp	7	4.8	±	0.7	4.6	±	0.3	4.0	±	0.8
Gln	8				4.1	±	0.4	2.2	±	0.6
Leu	9	3.4	±	0.3	3.2	±	0.3	4.4	±	0.6
Val	10	3.0	±	0.4	3.1	±	0.2	4.0	±	0.3
Leu	11	4.8	±	0.4	4.0	±	0.4	5.2	±	0.5
His	12	3.8	±	0.5	4.0	±	0.3	6.0	±	0.8
Val	13	2.4	±	0.4	2.6	±	0.3	4.1	±	0.6
Trp	14	4.6	±	0.4	4.8	±	0.3	7.0	±	0.5
Ala	15	3.8	±	0.5	4.0	±	0.4	3.5	±	0.5
Lys	16	2.9	±	0.4	3.2	±	0.3	6.5	±	0.4
Val	17	3.0	±	0.4	2.9	±	0.2	5.5	±	0.4
Glu	18	4.3	±	0.5	5.2	±	0.2	7.0	±	0.4
Ala	19	2.8	±	0.4	3.2	±	0.3	4.4	±	0.5
Asp	20	4.8	±	0.3	4.5	±	0.3	5.6	±	0.4
Val	21	3.6	±	0.5	3.7	±	0.4	4.2	±	0.7
Ala	22				4.1	±	0.4	0.9	±	0.4
Gly	23	5.0	±	0.4	5.6	±	0.3	3.6	±	0.3
His	24	4.1	±	0.4						
Gly	25	5.7	±	0.4	5.9	±	0.2	13.6	±	0.5
Gln	26				2.9	±	0.2	0.3	±	0.3
Asp	27	3.5	±	0.5	4.8	±	0.2	8.8	±	0.4
Ile	28	2.6	±	0.4	4.2	±	0.3			
Leu	29	2.6	±	0.4	5.3	±	0.2			
Ile	30	3.3	±	0.4	4.3	±	0.3			
Arg	31	2.7	±	0.3						
Leu	32	3.4	±	0.3	4.0	±	0.2	9.3	±	0.4
Phe	33	3.2	±	0.2	4.9	±	0.2			
Lys	34	4.0	±	0.3	4.3	±	0.2	9.5	±	0.4
Ser	35	3.2	±	0.4	3.7	±	0.3	1.7	±	0.3
His	36	4.8	±	0.4	4.7	±	0.2			
Glu	38	5.9	±	0.5	6.1	±	0.3	9.9	±	0.4
Thr	39	4.8	±	0.5	4.7	±	0.3	7.1	±	0.4
Leu	40	3.0	±	0.4	1.9	±	0.2	−8.4	±	0.4
Glu	41	3.4	±	0.4	4.7	±	0.2	10.3	±	0.3
Lys	42	3.8	±	0.4	5.1	±	0.3			
Phe	43	5.9	±	0.3	5.4	±	0.1			
Asp	44	5.6	±	0.5	5.8	±	0.3			
Arg	45	4.7	±	0.5	1.9	±	0.3			
Phe	46				2.7	±	0.1			
Lys	47	2.7	±	0.4	4.5	±	0.2	12.8	±	0.4
His	48	2.6	±	0.7	3.3	±	0.5			
Leu	49	3.7	±	0.5	2.9	±	0.2	−6.9	±	0.3
Lys	50	2.6	±	0.3	2.8	±	0.3	3.1	±	0.5
Thr	51	1.2	±	0.3	1.5	±	0.2	3.9	±	0.4

Table 2 continued.

		η^{CO} (s^{-1})			η^{CN} (s^{-1})			η^{F} (s^{-1})		
Glu	52	7.0	±	0.6						
Ala	53	3.7	±	0.3				2.9	±	0.5
Glu	54	4.0	±	0.2				6.9	±	0.3
Met	55	2.7	±	0.3	3.5	±	0.2			
Lys	56				4.0	±	0.2	3.4	±	0.3
Ala	57	3.2	±	0.4	3.8	±	0.3	5.0	±	0.4
Ser	58	3.9	±	0.4	4.4	±	0.2	5.6	±	0.4
Glu	59	5.3	±	0.5	4.7	±	0.5	4.6	±	0.5
Asp	60	4.0	±	0.4	3.2	±	0.3	3.0	±	0.4
Leu	61	4.9	±	0.4	3.2	±	0.2	−5.7	±	0.4
Lys	62	3.4	±	0.3				−6.9	±	0.3
Lys	63	4.6	±	0.5	4.3	±	0.2			
His	64				3.4	±	0.3			
Gly	65	5.5	±	0.5	3.8	±	0.2			
Val	66	2.5	±	0.3	3.4	±	0.2			
Thr	67	3.2	±	0.4	4.8	±	0.3			
Val	68	2.6	±	0.4	10.4	±	0.2			
Leu	69	2.5	±	0.2	6.6	±	0.2			
Thr	70				4.3	±	0.3			
Ala	71	2.9	±	0.4						
Leu	72	3.7	±	0.3	6.7	±	0.2			
Gly	73	5.9	±	0.4	6.5	±	0.2			
Ala	74	4.0	±	0.5	2.7	±	0.3			
Ile	75	2.0	±	0.3	1.4	±	0.2			
Leu	76	4.7	±	0.4	4.1	±	0.2	−2.1	±	0.4
Lys	77	4.7	±	0.5	3.5	±	0.3	−0.1	±	0.3
Lys	78				3.4	±	0.3	−2.9	±	0.3
Lys	79									
Gly	80				3.2	±	0.7	−5.2	±	0.6
His	81	5.0	±	0.4	5.5	±	0.2	8.9	±	0.3
His	82				−0.4	±	0.3	1.6	±	0.3
Glu	83	4.2	±	0.3	3.2	±	0.3	−2.2	±	0.5
Ala	84	4.7	±	0.3	5.0	±	0.5	2.5	±	0.3
Glu	85	3.7	±	0.4	3.2	±	0.3			
Leu	86									
Lys	87									
Leu	89	2.1	±	0.3	1.2	±	0.1			
Ala	90	5.2	±	0.4	3.2	±	0.1			
Gln	91	3.6	±	0.4	7.4	±	0.2			
Ser	92	3.3	±	0.4	8.7	±	0.2			
His	93	3.1	±	0.5						
Ala	94	4.6	±	0.5	8.4	±	0.2			
Thr	95	2.0	±	0.5	5.1	±	0.2			
Lys	96	2.4	±	0.4	3.0	±	0.2			
His	97	3.1	±	0.4	9.1	±	0.2			
Lys	98	2.5	±	0.4	7.9	±	0.3			
Ile	99				8.2	±	0.2			
Ile	101	5.4	±	0.4	4.0	±	0.2			
Lys	102	5.6	±	0.5				8.5	±	0.4
Tyr	103	4.7	±	0.4	6.7	±	0.2			

Table 2 continued.

		η^{CO} (s^{-1})			η^{CN} (s^{-1})			η^{F} (s^{-1})		
Leu	104				4.3	±	0.3			
Glu	105	3.6	±	0.4	2.9	±	0.3			
Phe	106				3.7	±	0.3			
Ile	107	4.0	±	0.5						
Ser	108				4.4	±	0.2			
Glu	109									
Ala	110	3.6	±	0.5	2.3	±	0.3	−3.6	±	0.5
Ile	111				2.9	±	0.2			
Ile	112	2.1	±	0.5				3.6	±	0.2
His	113	4.2	±	0.6	4.2	±	0.3			
Val	114	4.1	±	0.4						
Leu	115	4.0	±	0.4	3.3	±	0.3	1.9	±	0.5
His	116	4.8	±	0.4				2.1	±	0.3
Ser	117	3.9	±	0.4	4.2	±	0.3	0.9	±	0.6
Arg	118	4.4	±	0.5	4.1	±	0.3	0.9	±	0.5
His	119				4.0	±	0.2	3.2	±	0.3
Gly	121	5.0	±	0.8						
Asp	122	2.9	±	0.3						
Phe	123	2.1	±	0.3	2.4	±	0.2	2.2	±	0.3
Gly	124	5.2	±	0.4	5.4	±	0.4	5.1	±	1.5
Ala	125	5.4	±	0.5				5.2	±	1.5
Asp	126	2.3	±	0.6				1.8	±	0.8
Ala	127	3.2	±	0.5	2.9	±	0.4	2.9	±	0.7
Gln	128	4.3	±	0.3	3.9	±	0.3	2.6	±	0.5
Gly	129	5.0	±	0.4	4.8	±	0.3	4.4	±	0.6
Ala	130	3.6	±	0.4	4.2	±	0.3	3.2	±	0.6
Met	131	4.5	±	0.4	4.9	±	0.3	3.4	±	0.5
Asn	132	5.5	±	0.6				1.9	±	0.6
Lys	133	3.2	±	0.3						
Ala	134	4.9	±	0.4				6.2	±	0.4
Leu	135				3.5	±	0.3	1.6	±	0.4
Glu	136	3.6	±	0.5	3.8	±	0.3	0.9	±	0.4
Leu	137	4.5	±	0.5	4.9	±	0.2	8.4	±	0.5
Phe	138	3.4	±	0.4	3.9	±	0.1			
Arg	139	3.8	±	0.5	5.9	±	0.2			
Lys	140	4.5	±	0.8	4.5	±	0.3	8.9	±	0.5
Asp	141				6.1	±	0.3	12.7	±	0.4
Ile	142	3.8	±	0.3	4.8	±	0.2	14.0	±	0.3
Ala	143	4.9	±	0.5	6.4	±	0.2	14.4	±	0.3
Ala	144	3.4	±	0.3	4.2	±	0.3	10.2	±	0.4
Lys	145	3.5	±	0.4	3.3	±	0.2	4.0	±	0.3
Tyr	146	5.9	±	0.4	6.1	±	0.3	11.2	±	0.4
Lys	147				3.9	±	0.2	6.5	±	0.3
Glu	148	3.2	±	0.4	3.2	±	0.2	3.7	±	0.4
Leu	149				3.0	±	0.2	2.3	±	0.3
Gly	150	5.3	±	0.4	6.2	±	0.3	9.1	±	0.3
Tyr	151	4.3	±	0.3				6.7	±	0.3
Gln	152	3.8	±	0.4	4.5	±	0.4	8.6	±	0.6
Gly	153	0.8	±	0.6	1.6	±	0.4	3.6	±	0.6

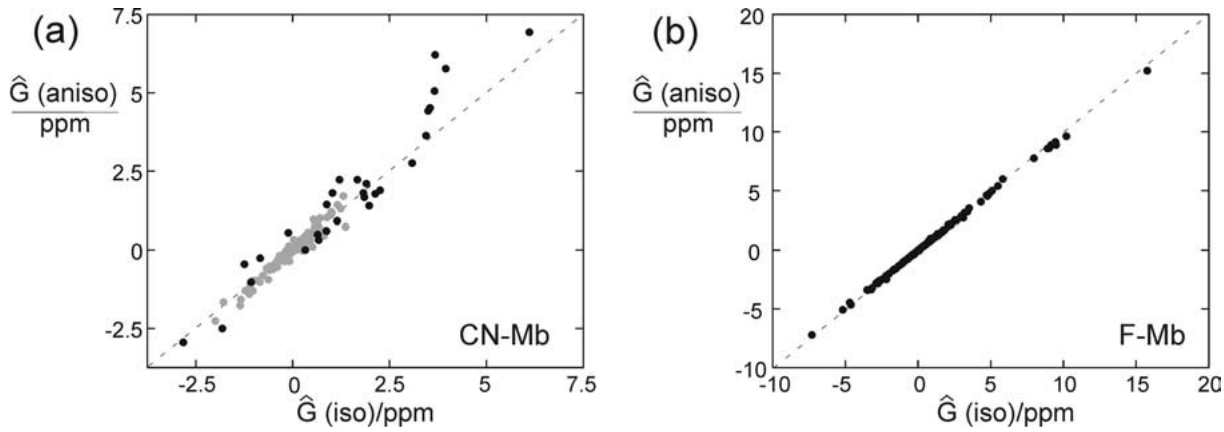

Figure 5. Correlations between the geometrical factors $\hat{G}$ calculated with the isotropic (Equation 9) and the anisotropic model (Equation 8) for CN-Mb (a) and F-Mb (b). Data points for protons located further than 11 Å from the metal are plotted in grey in the correlation plot of CN-Mb.

higher electronic spin in F-Mb should translate into correspondingly larger rates near the metal centre, these could not be measured, as those amides also exhibited higher paramagnetic auto-correlation rates and were not detectable in the ^{15}N-HSQC experiments. Notably, however, the larger radius of the effect in F-Mb allowed the measurement of many more significant DDxCSR rates, providing long-range structural information at distances between 10 and 25 Å from the metal (Figure 7b).

Figure 8 compares the experimentally determined DDxCSR rates with predictions made on the basis of Equations 8 and 9, using angles and distances derived from the crystal structure; data from the three N- and C-terminal residues were excluded from the analysis to avoid effects from large amplitude motions. An isotropic rotational correlation time τ_c of 5.7 $\pm$ 0.3 ns was used in the analysis. This value was derived from the ^{15}N T_1 and T_2 relaxation times measured for 25 α-helical residues of the CO-Mb sample.

For the high-spin myoglobin sample (Figures 8b and d), the correlations are good ($R = 0.97$), independent of the assumption of isotropic or anisotropic susceptibility, resulting in a slope that is unity within the uncertainty originating from the estimates of χ_{iso} and τ_c. This result was expected because the anisotropy in the susceptibility tensor is small (Table 1).

The quality of the correlation is worse in the case of the low-spin complex, independent of the assumption of an isotropic or anisotropic susceptibility tensor (Figures 8a and c). The correlation is, however, clearly better for the anisotropic than the isotropic model ($R =$ 0.95 *versus* 0.92; $R = 0.96$ *versus* 0.90 if calculated only for nuclei within 11 Å from the metal). In either case, the slopes reported in Figures 8a and c, are close to unity.

Angular restraints from dipole-dipole-Curie cross-correlation rates

A plot of the product $\eta \cdot r^3$ versus the angle θ formed between the H-N and the metal-proton vector yields the angular dependence of the cross-correlation measurements in a way that is independent of the metal-proton distance r (Figure 9).

Figure 9 shows that an anisotropic susceptibility tensor can substantially confound the evaluation of experimentally measured cross-correlation effects in terms of angular restraints. While the DDxCSR rates show a simple dependence on the angle θ in the isotropic case (Figures 9b and d), the anisotropic susceptibility tensor adds a dependence on the angular position of the H-N bond vector in the principal axes system of the susceptibility tensor. In the case of CN-Mb, the effect of this contribution produces significant deviations from the isotropic case, depending on the azimuthal position of the proton relative to the χ tensor main axis (θ_{zHFe}) and the orientation of the H-N bond with respect to the main axes of the susceptibility tensor (Figures 9a and c). As a result, the simple sinusoidal curve of the isotropic case becomes a belt of allowed values in the anisotropic situation, the width of which depends on the magnitude of the anisotropy parameters (Figure 9c). Consequently, the set of DDxCSR rates measured for F-Mb could be translated into θ angle restraints with much better accuracy than the corresponding data of CN-Mb (Figures 9c and d).

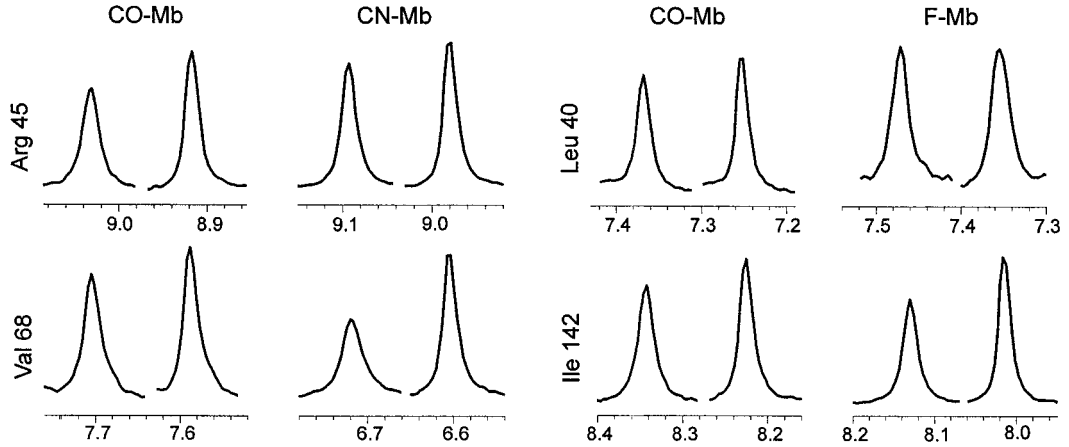

Figure 6. ^{1}H line shapes in the $^{1}H^{N}$ doublets for selected resonances in the three myoglobin complexes at 800 MHz. Displayed are the cross-sections along the F2 frequency axis of two different generalized ^{15}N-TROSY experiments (Weigelt, 1998) in which the two doublet components were recorded separately. DDxCSA effects consistently broaden the less-shielded doublet component and narrow the more-shielded component in diamagnetic CO-Mb. Depending on the orientation of the NH bond with respect to the metal ion, the additional DDxCSR effects in the paramagnetic CN-Mb and F-Mb samples can either compensate (top panel) or enhance (bottom panel) the line-shape effects from DDxCSA. The cross sections were scaled to present the more-shielded doublet components with similar height.

The strong distance dependence of the uncertainty in the product $\eta \cdot r^3$ further means that the reliability of the data decreases with increasing metal-proton distance r. For CN-Mb, the θ dependence could thus no longer be resolved for protons further than 11 Å from the metal (Figure 9c), as the DDxCSR rates measured became smaller than the experimental error. Notably, however, small cross-correlation rates can also result for protons close to the metal for angles θ_{zHFe} near the magic angle. In this case, small values convey meaningful angular information.

Discussion

Resonance assignment

The assignment of the ^{15}N-HSQC spectrum of CN-Mb presents the first example, where complete assignments of the ^{15}N-HSQC spectrum of a paramagnetic protein were obtained based on the strategy proposed by Tolman et al. (1995). This strategy relies on the availability of a 3D structure and assignments for the diamagnetic protein to obtain the assignments for the paramagnetic protein by a combination of NOE data and prediction of pseudo-contact shifts, circumventing the need of ^{13}C-labelling. The same strategy yielded the nearly complete assignment of the ^{15}N-HSQC spectrum of the high-spin sample, F-Mb. The protocol appears readily amenable to automation. The anisotropy and orientation of the metal susceptibility tensor can be calculated from a minimum of five pseudo-contact shifts identified in the spectrum or could be estimated from the electronic structure of the paramagnetic ion. Each new assignment allows refinement of the susceptibility tensor, improving the prediction of pseudo-contact shifts for the other cross-peaks.

Electronic properties and origin of anisotropic susceptibility

The different shapes of the susceptibility tensors in CN-Mb and F-Mb are consequences of the different electronic structures of the two iron spin states. Low-spin Fe(III) in an octahedral ligand field possesses an orbitally triply-degenerate ground state (Bertini and Luchinat, 1986). Anisotropic susceptibilities arise from highly anisotropic g tensors which are determined by the orbital contributions to the magnetic moment. The axial and rhombic parameters in Equation 1 are functions of the components of the electronic g tensor in the ground and excited states of the metal (Bertini et al., 2000). The orientation of the anisotropic susceptibility tensor is predominantly determined by the orientations of the axial ligands relative to the heme (Banci et al., 1995, 1996) and the deviation of the Fe-ligand vectors from the normal to the heme-plane (Nguyen et al., 1986).

High-spin ferric heme proteins have an orbitally non-degenerate, spherically symmetric ground state (Bertini and Luchinat, 1986); this implies that the g tensor is isotropic. The (generally less pronounced)

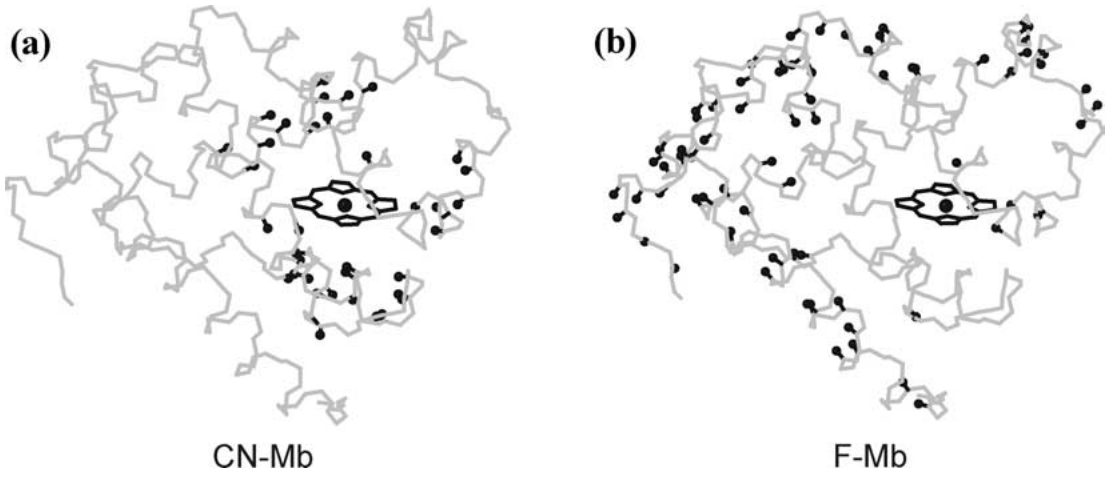

Figure 7. Backbone representations (gray lines) of myoglobin with the HN vectors for which significant DDxCSR effects could be measured. For CN-Mb (a) the effect vanished at a distance of about 11 Å from the metal ion, while a region between 10 and 25 Å could be examined in the case of F-Mb (b).

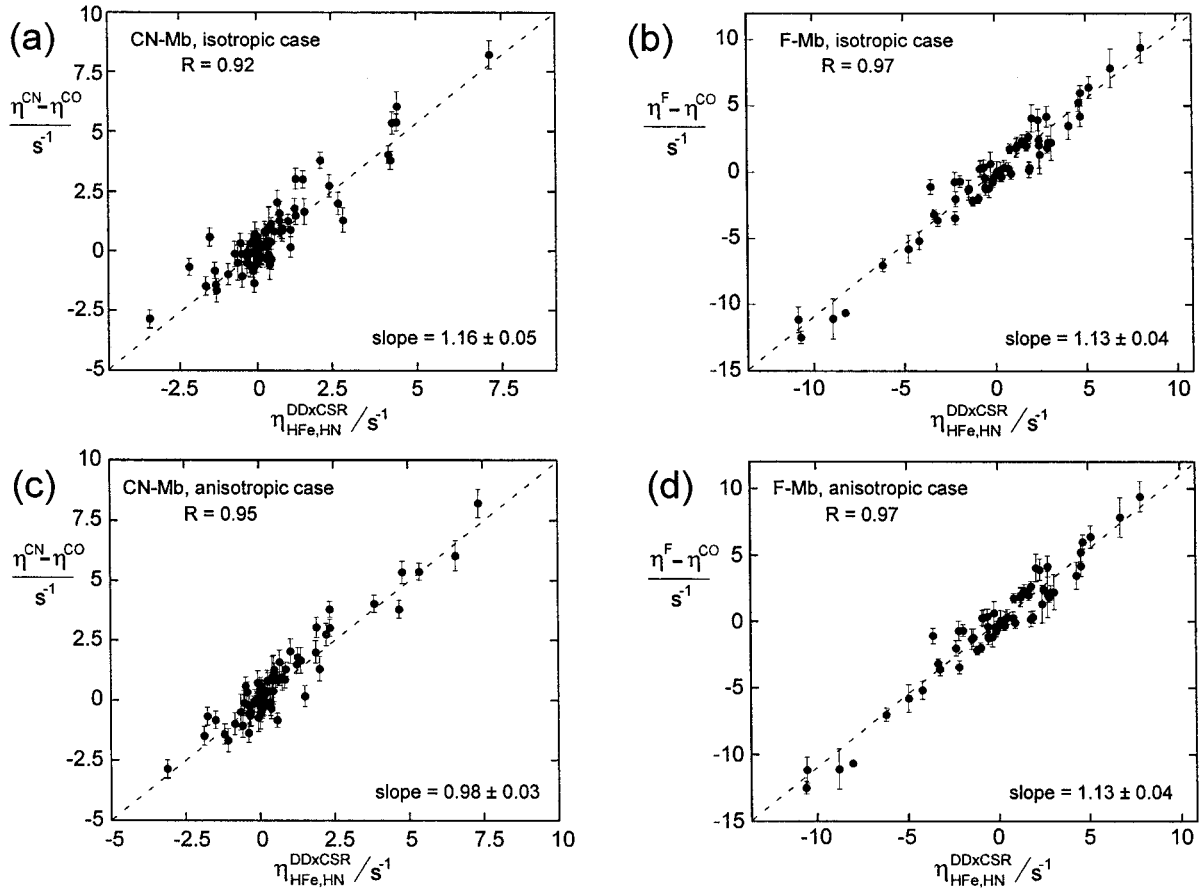

Figure 8. Correlation between experimentally determined and predicted DDxCSR rates. (a) CN-Mb, assuming an isotropic susceptibility tensor; (b) F-Mb, assuming an isotropic susceptibility tensor; (c) CN-Mb, assuming an anisotropic susceptibility tensor; (d) F-Mb, assuming an anisotropic susceptibility tensor. For each plot, the fitted linear correlation is reported (dashed line), together with its slope and the correlation coefficient *R*. Orientations and magnitudes of the susceptibility tensors used are given in Table 1. The data of all assigned cross peaks are included in the plots.

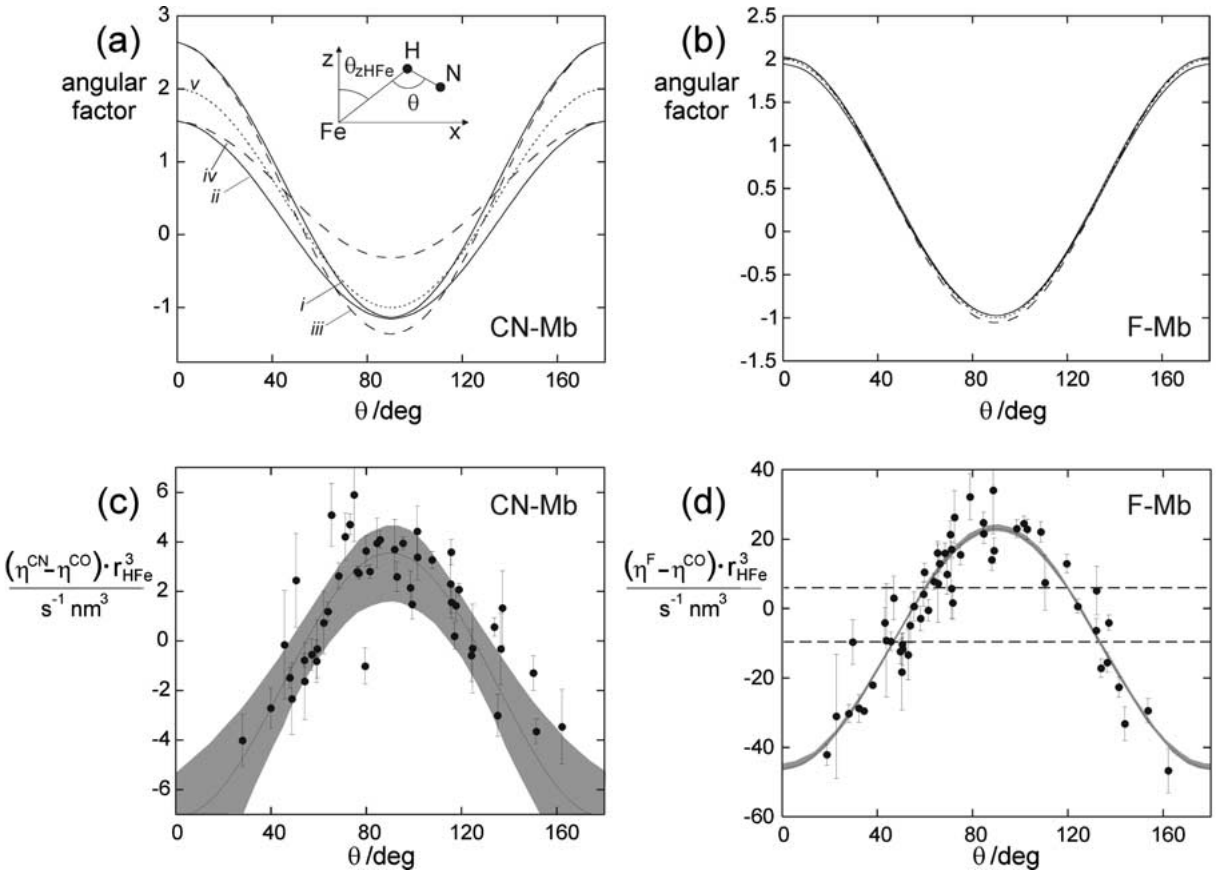

Figure 9. Angular dependence of DDxCSR rates. (a) and (b) Predicted effect of anisotropic magnetic susceptibility on the ratio $\hat{G}$ as a function of the angle θ between the H-N and H-Fe vectors (insert in (a)) for CN-Mb and F-Mb, respectively. In the isotropic case, the ratio between the geometric factor $\hat{G}$ and the axial dipolar shift of the isotropic case $\Delta\sigma(iso)$ is equivalent to the angular factor *3 cos*^{2}θ*-1* (Bertini et al., 2001). Curves were calculated for different geometries. The proton was fixed in the plane determined by the *x* and *z* components (smallest and largest) of the metal χ tensor, at an azimuthal angle θ_{zHFe} from the *z* axis, while the H-N vector was rotated through all possible angles θ with respect to the H-Fe vector. The curves shown were calculated for $\theta_{zHFe} = 0°$ (*i* and *ii*, solid lines) and $\theta_{zHFe} = 90°$ (*iii* and *iv*, dashed lines), with the H-N vector lying within the xz-plane (*i* and *iii*) or in a plane perpendicular to the *xz*-plane (*ii* and *iv*). The corresponding result for the isotropic susceptibility tensor is also displayed (dotted line *v*). In the case of F-Mb, all the simulated curves are very close to each other. (c) and (d) Angular dependence of the products $\eta \cdot r^3_{HFe}$, where η is the DDxCSR rate, plotted for CN-Mb and F-Mb, respectively. Because of the contribution of the anisotropic χ tensor, allowed regions of the plot are not confined to the single curve of the isotropic case (continuous line), but span a larger area (shaded regions) which is especially wide for CN-Mb (c). The plots include only experimental points with reasonably small error margins. Two horizontal lines in (d) delineate the range of values predicted for CN-Mb (c).

pseudo-contact shifts arise from a significant zero-field splitting (ZFS), i.e., the susceptibility values of Equation 1 are related to the axial zero-field splitting parameter with negligible rhombic parameter (Bertini and Luchinat, 1986).

In principle, the unpaired spin density of electrons is not confined to the metal centre but partly delocalized over the heme ring. However, π spin delocalization, which could strongly affect the nuclear spins of the ligand, is unimportant in low-spin Fe(III) complexes, so that the effects from the electron paramagnetism of the metal are well approximated by a point-dipole model even for nuclei which are very close to the metal ion, as long as contact effects are negligible (Nguyen et al., 1993). The validity of this approximation is underscored by the close agreement between experimentally observed and predicted pseudo-contact shifts for all amide groups except that of the directly coordinated His 93.

In contrast, σ delocalization is large in high-spin Fe(III) heme complexes, so that the point-dipole model presents an acceptable approximation only for nuclei more than 10 Å away from the metal (Golding et al., 1976). As the signals from closer amide pro-

tons were anyway broadened beyond detection, this criterion was satisfied by all backbone nuclei of F-Mb evaluated in the present work.

The different electronic structure of the metal ion further results in different electronic relaxation rates τ_e for the two spin states, with τ_e of about 10^{-12} and 10^{-10} s for low- and high-spin iron, respectively (Bertini and Luchinat, 1986). Both relaxation rates are much shorter than the rotational correlation time τ_c. Therefore, the CSR rate is independent of the electronic relaxation rate and the longer relaxation time of the high-spin iron is important only for other mechanisms contributing only to the auto-correlated relaxation rate λ. These contributions enhance the observed line broadening beyond that caused by the Curie spin interaction.

Dipole-dipole-Curie-spin cross-correlation rates

The number of amide cross-peaks for which quantitative cross-correlation rates could be measured was significantly smaller than the number of observable HSQC cross-peaks, although no signals were lost during the longer pulse sequence used for relaxation measurements. As the measurements required the evaluation of cross-peak intensities in the paramagnetic and the diamagnetic sample, only cross-peaks that were resolved in both spectra could be evaluated. Furthermore, most of the DDxCSR rates measured in CN-Mb were smaller than the experimental error, because of the small magnitude of the electronic magnetic moment which is proportional to $S(S + 1)$.

The longer range of the effects of paramagnetism in the F-Mb complex provided a complementary set of data. Although fewer peaks were detected in the ^{15}N-HSQC spectrum of F-Mb due to paramagnetic line broadening, the larger paramagnetism yielded more angular restraints, since all the measured cross-correlation rates at larger distances possessed smaller relative uncertainties (note the different vertical scales in Figure 9, c and d). On the other hand, as measurable DDxCSR effects were found closer to the metal in the low-spin complex than in the high-spin complex, the low-spin complex is more sensitive to structural differences near the metal, providing conformational probes close to the active site of the protein. In either situation, the experimental uncertainty of the angular restraints scale with r^3 with increasing distance from the metal ion (Figures 9c and d) which needs to be considered when the cross-correlation information is translated into angular restraints for structure calculations.

The lower quality of the correlation between experimental and calculated cross-correlation rates obtained for CN-Mb seems best explained by small conformational differences between the crystal structure of CO-Mb used for predicting the effects and the solution structure of CN-Mb. Small differences near the ligand-binding site are expected to arise from the different axial coordination of the CN and CO ligands (PDB codes 1EBC and 1BZR, respectively; Bolognesi et al., 1999; Kachalova et al., 1999) and would, in solution, mostly be confined to the vicinity of the metal ion. Furthermore, the functional shape of the cross-correlation term (Equation 8 or 9) is particularly sensitive to structural variations at short metal-to-proton distances r_{HFe}. This effect would also render the DDxCSR rates of amide groups near the metal centre more susceptible to dynamic averaging between different conformations than those of remote amide groups.

Anisotropy effects in dipole-dipole-Curie-spin cross-correlation

The anisotropic susceptibility tensor in CN-Mb adds significant uncertainty to the angular restraints obtained from the experimentally measured DDxCSR effects (Figure 9c). The set of DDxCSR rates measured for F-Mb can be translated into θ angle restraints with much better accuracy (Figure 9d).

The effects arising from an anisotropic susceptibility tensor are small, if the magnetic anisotropy is at least one order of magnitude smaller than the average susceptibility. Therefore, hardly significant anisotropy corrections may be expected for, e.g., lanthanide complexes where large anisotropy effects are superimposed on large isotropic susceptibilities. As shown here, however, cross-correlation data from low-spin iron complexes can be affected significantly by anisotropy effects. The phenomenon is expected to be important also for other heteronuclei of similar isotropic susceptibility and low electronic magnetogyric ratio for which NMR spectra can be recorded closer to the paramagnetic centre. Anisotropy effects may also be relevant for other highly anisotropic metal ions such as high-spin cobalt (II).

Conclusions

The present work shows how different spin states of the same metal can be exploited to get long-

range structural information at variable distance from a metal center from cross correlated relaxation rates. The approach presents an alternative to experiments with different lanthanide ions (Allegrozzi et al., 2000), where the electronic spin state can be tailored by the use of different metals endowed with different magnetic anisotropies.

This is the first time that the effect of anisotropic magnetic susceptibility on DDxCSR has been shown to be experimentally significant. While the effect could be neglected in the model systems studied in the past, such as in the example of Cerium(III)-substituted Calbindin D^{9k} (Bertini et al., 2002a), it is no longer negligible for low-spin CN-Mb, where the iron displays at the same time a small average susceptibility and large anisotropy magnitudes.

Acknowledgements

The authors thank Jozef Kowalewski, Isabella Felli, Mario Piccioli and P.K. Madhu for helpful discussions, Giacomo Parigi for support in the calculations, Simone Zaramella and Irena Matecko for help in the preparation of the CO-Mb sample, the Knut and Alice Wallenberg Foundation for access to an 800 MHz NMR spectrometer and Johan Weigelt for help on the spectrometer. G.P. thanks the EU for a postdoctoral fellowship within the Research Training Network on Cross-Correlation (HPRN-CT-2000-00092). G.O. acknowledges a Federation Fellowship from the Australian Research Council. Financial support by the Swedish Research Council and the Austrian Science Funds (FWF, project P15380) is gratefully acknowledged. Initial NMR experiments at 800 MHz were recorded at the EU large scale facilities for biomolecular NMR in Frankfurt and Florence, supported by the projects HPRI 1999-CT-00014 and HPRI-CT-1999-00009.

References

Aime, S., Fasano, M., Paoletti, S., Cutruzzolà, F., Desideri, A., Bolognesi, M., Rizzi, M. and Ascenzi, P. (1996) *Biophys. J.*, **70**, 482–488.

Allegrozzi, M., Bertini, I., Janik, M.B.L., Lee, Y.-M., Liu, G. and Luchinat, C. (2000) *J. Am. Chem. Soc.*, **122**, 4154–4161.

Banci, L, Pierattelli, R. and Turner, D.L. (1995) *Eur. J. Biochem.*, **232**, 522–527.

Banci, L., Rosato, A. and Turano, P. (1996) *JBIC*, **1**, 364–367.

Bartels, C., Xia, T.H., Billeter, M., Güntert, P. and Wüthrich, K. (1995) *J. Biomol. NMR*, **6**, 1–10.

Beetlestone, J. and George, P. (1964) *Biochemistry*, **3**, 707–714.

Bertini, I. and Luchinat, C. (1986) *NMR of Paramagnetic Molecules in Biological Systems*, The Benjamin/Cummings Publishing Co., Menlo Park, NJ.

Bertini, I. and Luchinat, C. (1996) *Coord. Chem. Rev.*, **150**, 1–292.

Bertini, I., Cavallaro, G., Cosenza, M., Kümmerle, R., Luchinat, C., Piccioli, M. and Poggi, L. (2002a) *J. Biomol. NMR*, **23**, 115–125.

Bertini, I., Luchinat C. and Parigi, G. (2002b) *Prog. NMR Spectrosc.*, **40**, 249–273.

Bertini, I., Kowalewski, J., Luchinat, C. and Parigi, G. (2001) *J. Magn. Reson.*, **152**, 103–108.

Bertini, I., Luchinat, C. and Parigi, G. (2000) *Eur. J. Inorg. Chem.*, 2473–2480.

Bertini, I., Luchinat, C., Piccioli, M. and Tarchi, D. (1994) *Concepts Magn. Reson.*, **6**, 307–335.

Bertini, I., Luchinat, C. and Tarchi, D. (1993) *Chem. Phys. Lett.*, **203**, 445–449.

Bertini, I., Luchinat, C. and Vasavada, K.V. (1990) *J. Magn. Reson.*, **89**, 243–254.

Boisbouvier, J., Gans, P., Blackledge, M., Brutscher, B. and Marion, D. (1999) *J. Am. Chem. Soc.*, **121**, 7700–7701.

Bolognesi, M., Rosano, C., Losso, R., Borassi, A., Rizzi, M., Wittenberg, J.B., Boffi, A. and Ascenzi, P. (1999) *Biophys. J.*, **77**, 1093–1099.

Cerdonio, M., Morante, S. and Vitale, S. (1981) *Meth. Enzymol.*, **76**, 354–371.

Delaglio, F., Grzesieck, S., Vuister, G., Zhu, G., Pfeifer, J. and Bax, A. (1995) *J. Biomol. NMR*, **6**, 277–293.

Desvaux, H. and Gochin, M. (1999) *Mol. Phys.*, **96**, 1317–1333.

Di Bari, L., Pintacuda, G., Ripoli, S. and Salvatori, P. (2002) *Magn. Reson. Chem.*, **40**, 396–405.

Emerson, S.D. and La Mar, G.N. (1990) *Biochemistry*, **29**, 1556–1566.

Fann, Y.-C., Ong, J.-L., Nocek, J.M. and Hoffman B.M. (1995) *J. Am. Chem. Soc.*, **117**, 6109–6116.

Farrow, N.A., Muhandiram R., Singer, A.U., Pascal, S.M., Kay, C.M., Gish, G., Shoelson, S.E., Pawson, T., Forman-Kay, J.D. and Kay, L.E. (1994) *Biochemistry,* **33**, 5984–6003.

Geen, H. and Freeman, R. (1991) *J. Magn. Reson.*, **93**, 93–141.

Ghose, R. and Prestegard, J.H. (1997) *J. Magn. Reson.*, **128**, 138–143.

Golding, R., Pascual, R. and Stubbs, L. (1976) *Mol. Phys.*, **31**, 1933–1938.

Goldman, M. (1984) *J. Magn. Reson.*, **60**, 437–452.

Guéron, M. (1975) *J. Magn. Reson.*, **19**, 58–66.

Güntert, P., Dötsch, V., Wider, G. and Wüthrich, K. (1992) *J. Biomol. NMR*, **2**, 619–629.

Hus, J.-C., Marion, D. and Blackledge, M. (2000) *J. Mol. Biol.*, **298**, 927–936.

Jennings, P.A., Stone, M.J. and Wright, P.E. (1995) *J. Biomol. NMR*, **6**, 271–276.

Johnson, B.A. and Blevins, R.A. (1994) *J. Biomol. NMR*, **4**, 603–614.

Kachalova, G.S., Popov, A.N. and Bartunik, H.D. (1999) *Science* **284**, 473–476.

Kao, Y.-H. and Lecomte, J.T.J. (1993) *J. Am. Chem. Soc.*, **115**, 9754–9762.

Koradi, R., Billeter, M. and Wüthrich, K. (1996) *J. Mol. Graphics*, **14**, 51–55.

Madhu, P.K., Grandori, R., Hohenthanner, K., Mandal, P.K. and Müller, N. (2001), *J. Biomol. NMR*, **20**, 31–37.

Madhu, P.K., Mandal, P.K. and Müller, N. (2002) *J. Magn. Reson.*, **155**, 29–38.

Mandal, P.K., Madhu, P.K. and Müller, N. (2000) *Chem. Phys. Lett.*, **320**, 269–276.

Mandel, A.M., Akke, M. and Palmer, A.G. (1995) *J. Mol. Biol.*, **246**, 144–163.

Nguyen, B.D., Xia, Z., Yeh, D.C., Vyas, K., Deaguero, H. and La Mar, G.N. (1999) *J. Am. Chem. Soc.*, **121**, 208–217.

Nocek, J.M., Huang, K. and Hoffman, B.M. (2000*) Proc. Natl. Acad. Sci. USA*, **97**, 2538–2543.

Ösapay, K., Thériault, Y., Wright, P.E. and Case, D.A. (1994) *J. Mol. Biol.*, **244**, 183–197.

Phillips, Jr., G.N. (2001) In *Handbook of Metalloproteins*, Messerschmidt, A., Huber, R., Wieghardt, K. and Poulos, T. (Eds.), Wiley, New York, NY.

Qin, J., Delaglio, F., La Mar, G.N. and Bax, A. (1993) *J. Magn. Reson.*, **B102**, 332–336.

Qin, J., La Mar, G.N., Ascoli, F. and Brunori, M. (1993) *J. Mol. Biol.*, **231**, 1009–1023.

Sharma, Y., Kwon, O.Y., Brooks, B. and Tjandra, N. (2002) *J. Am. Chem. Soc.*, **124**, 327–335.

Sklenár, V., Piotto, M., Leppik, R. and Saudek, V. (1993) *J. Magn. Reson.*, **A102**, 241–245.

Thériault, Y., Pochapsky, T.C., Dalvit, C., Chiu, M.L., Sligar, S.G. and Wright, P.E. (1994) *J. Biomol. NMR*, **4**, 491–504.

Tolman, J.R., Flanagan, J.M., Kennedy, M.A. and Prestegard, J.H. (1995) *Proc. Natl. Acad. Sci. USA*, **92**, 9279–9283.

Turano, P. and Lu, Y. (2001) In *Handbook on Metalloproteins*, Bertini, I., Sigel, A. and Sigel H. (Eds.), Dekker, Basel.

Vega, A.J. and Fiat, D. (1976) *Mol. Phys.*, **31**, 347–351.

Vasavada, K.V. and Rao, B.D.N. (1989) *J. Magn. Reson.*, **81**, 275–283.

Weigelt, J. (1998) *J. Am. Chem. Soc.*, **120**, 10778–10779.